# Aero-Sol-Gel (ASG) Reactor For Nano-Powder Synthesis

G. Beaucage, J. Hyeon-Lee, D. J. Kohls

*Department of Materials Science and Engineering*

S. E. Pratsinis

*Department of Chemical Engineering*

*University of Cincinnati, Cincinnati, OH 45221-0012*

**Abstract:**

This paper discusses a new approach to the synthesis of nano-structured oxides where sol-gel reactions are carried out in aerosol droplets. This aero-sol-gel reactor (ASG) allows for manipulation of the structure, chemical composition and surface area of silica powders through variation of process parameters. ASG powders differ structurally from other continuous process powders such as pyrolytic and solution-route powders. ASG powders contain meso- and micropores, the mesopores being responsible for high surface areas measured by nitrogen adsorption using BET theory. Under controlled reaction conditions the powder structure is reproducible as measured by small-angle x-ray scattering, SAXS, analysis. The ASG reactor displays transport effects similar to those previously seen in laminar flame reactors as evidenced by the effect of reactor geometry and reactant concentration on product structure.

**Introduction:**

Previously we reported a new reactor for the production of silica and titania oxide powders with nano-scale structure and high specific surface areas (100 to 700 $m^2/g$) [1, 2]. This aero-sol-gel reactor (ASG) is similar in design to laminar flow pyrolytic reactors such as those reported by Pratsinis and coworkers [3-5]. The ASG reactor differs from these flame reactors first in that there is *no flame* present. Instead, oxide powders are produced by an *ambient temperature and pressure* hydrolysis/condensation chemical reaction which occurs simultaneous with thermal condensation of precursor vapor streams to an aerosol. The precursor vapor streams are fed into a mixing zone from a heated laminar flow assembly. Since no flame is present, the assembly is made of low-

cost, plastic tubing rather than the high temperature materials needed in flame reactors. Formation of metal oxides at ambient temperatures avoids sintering of primary particles and the associated reduction in specific surface area [6]. Byproduct removal from these powders occurs in a rapid, continuous manner, coincident with condensation of the precursor streams into a fine aerosol. Simultaneous aerosol condensation and reaction, alleviates pore collapse on drying common to room temperature solution processes [7].

The concept of chemical reactions in aerosols aimed at ceramic oxide production has precedence in the work of Egon Matijevic at Clarkson University [8-10]. Matijevic produced an aerosol stream of alkoxide precursors and humidified the aerosol in a reaction chamber. One aim of Matijevic's efforts was to produce close to monodisperse *sub-micron-scale* particles (0.1 to 1.0 μm) by process control over the aerosol droplet size [11]. Matijevic's aerosol reactor differs from the ASG reactor in that Matijevic's alkoxide aerosol is formed *prior to* reaction. Much of Matijevic's work involved production of amorphous titania particles which could be transformed into anatase or rutile by annealing in a separate stage. Matijevic also studied mixed oxides [10].

In the ASG reactor, aerosol formation occurs simultaneous with mixing of reactant vapor streams and initiation of oxide production. It is believed that this co-condensation of mixed reactant vapors is advantageous for production of aerogel-like nano-structure in ASG powders. Several other groups have used Matijevic-type aerosol reactors, with pre-formed alkoxide aerosols, using different techniques for aerosol formation such as jet nozzles [12-17]. The specific surface area of oxide particles produced from these pre-formed aerosol streams is less than 100 $m^2/g$. The ASG powders, reported here, generally display specific surface areas in the 400 to 700 $m^2/g$ range indicating that they may have a distinct structure from processes where a pre-formed alkoxide aerosol is used. Additionally, the ASG reactor appears to have a lower reaction temperature, close to room temperature, in comparison to the Matijevic-type reactors.

This paper discusses a control series of powders produced in the ASG Reactor from an acid catalyzed (HCl) hydrolysis/condensation reaction of tetraethoxysilane (TEOS) and water. Oxide growth from such sol-gel reactions can be categorized into: (1) dense, 3-d, surface-fractal

growth under *reaction-limited, monomer-cluster* conditions, or (2) ramified, low-dimensional, mass-fractal growth under *transport limited* conditions [6,7]. In the TEOS/HCl/Water system, hydrolysis of the alkoxide is accelerated by the presence of HCl [7]. Condensation of the resulting $Si(OH)_4$ and partial condensates, $Si(OH)_x(OC_2H_5)_{(4-x)}$ is a slower reaction than hydrolysis under acidic conditions. Nevertheless, in solution reactions, if sufficient acid catalyst is present to fully hydrolyze TEOS to $Si(OH)_4$, the condensation rate to silica is faster than the transport rate of hydrolyzed TEOS in the solution and the reaction is *transport-limited*, i.e. acid catalyzed hydrolysis/condensation leads to low-dimension mass-fractal aggregates [7, 18-20].

If insufficient HCl is present, it is likely that partial hydrolysis of TEOS occurs. Partially hydrolyzed TEOS is less likely to condense to silica in growing aggregates since fewer condensable -OH sites are available. It is expected that in partially condensed TEOS the formation of aggregates might exhibit a transition from low- to high-dimension growth, i.e. denser growth, as the degree of TEOS hydrolysis is reduced and as the formation mechanism changes from transport-limited to *reaction-limited*.

In addition to catalyst availability, a second process parameter, the water/TEOS molar ratio, governs silica growth. The ASG powders, discussed in this paper, use an overall water/TEOS molar feed ratio far in excess of stoichiometric. 2 moles of water are produced in the condensation step per mole $Si(OH)_4$, and 4 moles of water are consumed in the hydrolysis step for a net stoichiometric consumption of 2 moles water per mole TEOS in the overall reaction [7]. The presence of much higher concentrations of water than stoichiometric in hydrolysis/condensation reactions can lead to inhibition of condensation. In the ASG reactor, the three components of the hydrolysis/condensation reaction must meet in nascent aerosol droplets. High water content may serve to enhance transport of HCl to water, and to the reaction zone, depending on the lamellar flow stream configuration (Figure 1). HCl is much more miscible in water than TEOS, so acidified water serves as a conduit to bring the three components together.

Therefore, high water content in the ASG reactor can possibly lead to two different structural results, 1) High-water concentration can serve to enhance HCl transport and lead to

complete hydrolysis of TEOS and *transport-limited*, low-dimension aggregates, 2) high water content can inhibit the condensation reaction leading to *reaction-limited* growth and 3-d, solid aggregates. The data presented in this paper supports the first prediction in most cases, meaning that only a limited amount of the water fed to the reaction zone actually finds its way to the reacting, nascent aerosol droplets.

**Experimental:**

The ASG reactor consists of dry nitrogen streams bubbled through precursor liquids to form vapor streams. These bubblers can be heated to control the reactant concentration in the feed streams. In the formation of silica from tetraethoxysilane (TEOS), three vapor streams are fed into a laminar flow assembly: TEOS, water and HCl. All process vapor streams are heated to about 110°C to prevent premature condensation. The laminar flow streams feed into an open air mixing/condensation/reaction zone similar in design to pyrolytic reactors [1-6]. Nano-structured powders are collected in an inverted funnel filter connected to an adjustable vacuum through an aqueous NaOH solution bubbler. Figure 1 shows a schematic of the heated laminar flow assembly. Mixing of the reactant vapors depends initially on cross-flow diffusion between the laminar flow vapor streams entering the mixing zone. The details of this transport presumably effect the structure of the resulting nano-structured powders. The carrier gas flow rates (dry nitrogen) to all reactants is fixed at 45 $cm^3$/sec in the control study reported here.

In this paper we first report on variation of the arrangement of these three reactant streams in order to demonstrate that laminar flow configuration can be used to manipulate the ASG process. A study is presented of narrowly controlled reaction conditions for TEOS precursor streams in order to understand some of the processing features of the ASG reactor. (In a previous publication we demonstrated the wide range of structures which can be generated in this reactor [1].) Figure 1 shows the three different precursor laminar flow arrangements used in this study. In *Reactor Configuration A*, stream "c" was the alkoxide (TEOS), "b" was water and "a" was the catalyst, HCl. In *Reactor Configuration B*, stream "c" was the catalyst, HCl, "b" the alkoxide, and "a" water. In *Reactor Configuration C* stream "b" was again the alkoxide (TEOS), streams "a" and

"c" were exchanged from *Reactor Configuration B.*

Diffusive or convective transport probably occurs, initially, through vapor phase diffusion across laminar flow streams in the lower part of the mixing region. Transport of HCl and $H_2O$ is expected to occur at a much higher rate than diffusive transport of the heavier TEOS molecules, molar mass ratio of TEOS/$H_2O$ = 11.6.

Stream "a" can diffuse/convect either to the stagnant surrounding air or into the reaction zone, i.e. towards stream "c". Stream "b" is surrounded by two laminar flow streams and is not subjected to significant convective flow at the first stages of the mixing zone. Stream "c" is surrounded on all sides by the lateral reaction zone.

On entering the mixing zone, laminar streams cool to about 25°C due to contact with the surrounding air. A cooling gradient is created in the laminar outflow from the thermally controlled laminar flow assembly. The high dew-point vapors condense into aerosol droplets when the temperature drops and this initially occurs in the outer laminar stream, stream "a". Stream "a" vapors are most likely to serve as nuclei for aerosol formation from the other components when it contains water or alkoxy vapors but not for HCl since HCl is a gas at atmospheric pressure and ambient temperatures. When stream "a" is HCl gas it is expected that stream "b" will first condense and serve as nucleation site for stream "c". HCl is miscible with water but only marginally miscible with TEOS. Because of this, acidification of the reactants occurs at a later stage in *Reactor Configurations B* and *C* compared to *Reactor Configuration A.*

The three reactor schemes can be interpreted as:

*Reactor Configuration A*- Acidified water (a and b in Figure 1) first nucleates into aerosol droplets on which TEOS vapors (c) nucleate and condense.

*Reactor Configuration B*- Water (a) initially condenses into an aerosol, forming nuclei on which TEOS (b) condenses. This is similar to *Reactor Configuration A* except that the water aerosol is not initially acidified. The TEOS stream (b) may delay HCl (c) transport, but HCl is confined to the reaction zone since it is the central stream. This is less advantageous to hydrolysis than the scheme of *Reactor Configuration A.*

*Reactor Configuration C*- TEOS (b) condenses into aerosol droplets first. These TEOS droplets serve as seeds for water (c) condensation. The TEOS stream (b) may delay transport of HCl (a). HCl is **not** confined to the reaction zone since it is stream "a", i.e. the HCl stream can migrate to the surrounding air and become diluted. This is the least advantageous arrangement for the hydrolysis/condensation mixture.

In addition to variability in the mixing configuration, the concentration of reactants can be varied in an atmospheric pressure reactor through changes in the temperature of the precursor streams. For TEOS the alkoxide temperature was varied from 70°C to 90°C in all of the reactor configurations. The water temperature was varied from 75 to 90°C. These ranges were determined by the atmospheric boiling points of the precursors (168°C for TEOS) and by conditions under which powder was significantly produced, i.e. when the water temperature was below 65°C it was difficult to reproducibly obtain powder from the reactor.

As vapors proceed into the mixing/reaction zone and begin to condense, the condensation reaction forms extremely small nascent oxide particles on the 1 to 5 nanometer scale. Further downstream, growth continues in an environment where convection becomes more important and the effects of laminar flow become smeared by combined cross-flow diffusion and convective turbulence of the reactant streams. As noted above, the TEOS stream is composed of high molar-mass molecules with low transport coefficients. Water and HCl have comparable transport coefficients and are primarily responsible for cross-flow diffusion.

The HCl stream is produced by bubbling $N_2$ through an ambient-temperature, concentrated aqueous solution of HCl (38% HCl). The azeotrope for this solution is about 20% HCl so this process results in a vapor stream of primarily HCl. At 25 °C the vapor pressure of water from a 38% HCl solution is 3.60 mm Hg [21, p. 3-62] and the vapor pressure of HCl is 277 mm Hg [21, p. 3-63].

The molar concentration of water and TEOS vapor fed to the laminar flow chamber varies with the temperature of the reactant bubblers [21, 22, 32]. Tables 1 and 2 list the vapor pressures of the reactants and the estimated overall molar ratio of water and TEOS present for the reaction in

the mixing zone at 25°C [32, 22]. A stoichiometric mixture would involve an $H_2O$/TEOS ratio of 2. It was observed that in order to reproducibly produce powder, the feed rate of water must be significantly above this stoichiometric level as is the case for all of the reactions listed in Tables 1 and 2. In tables 1 and 2 the values at 25°C (Mixing Zone) are in italics and the standard reactor conditions of water at 75°C and TEOS at 85°C are in bold.

The hydrolysis/condensation reaction produces ethanol as a byproduct. At 26°C the vapor pressure of ethanol is 60 mmHg [21, p. 3-54]. Ethanol has a boiling point of 78.4 °C. This significant room temperature vapor pressure in the continuous flow reactor is sufficient for rapid ethanol byproduct removal if the reactants are well mixed in the mixing zone. Since water is present at close to saturated vapor pressure in the mixing zone, removal of excess water from the product is not favorable and we expect to see hydrated silica as a product. Additionally, there is probably post-aggregation hydrolysis in the ASG powders to fully hydrolyze TEOS in all powders since HCl is present with excess water. That is, for partially hydrolyzed TEOS under limited HCl conditions, aggregates may form from the partially hydrolyzed TEOS which age in the presence of excess water and some HCl to fully hydrolyzed TEOS.

**Results/Discussion:**

ASG powders show unique mesoporous to microporous structures for a continuous process synthesis. The ASG nano-structure is reminiscent of supercritically extracted aerogel powders. This can be shown by a comparison of small-angle x-ray scattering data from a series of silicas produced by different synthetic routes, Figure 2. In a small-angle x-ray scattering pattern the scattered intensity (arbitrarily scaled in Figure 2) is plotted as a function of the scattering vector, "q", which is a reduced scattering angle ($\theta$), $q = 4\pi/\lambda \sin(\theta/2)$, where $\lambda$ is the wavelength (here 1.54Å). "q" has units of inverse size and reflects the inverse of a Bragg-size, $d = 2\pi/q$, i.e. large "q" is associated with small size. The data of Figure 2 are typical of pinhole SAXS cameras and covers a size range from about 0.2 nm, at high-q, to about 50 nm, at low-q. This corresponds to the microporous to mesoporous ranges described in the gas adsorption literature [23]. The cut-off

size for micropores is about 2 nm in diameter which corresponds to about $q = 0.15Å^{-1}$ in Figure 2, i.e. micropore structure is observed for $q>0.15Å^{-1}$ and mesopore structure for $q<0.15Å^{-1}$.

Power law decays of intensity versus q are common to small-angle scattering data. Generally, slopes shallower than -3 (here -2.4 to -3.0) are considered mass-fractal, that is, they are associated with ramified structures which display mass-fractal scaling whose mass-fractal dimension, $d_f$, is the negative of the power-law slope [24]. Intensity that decays with power-law slopes steeper than -3 (here -3.0 to -3.4) are associated with surface scattering from rough surfaces [29-31]. The surface-fractal dimension is obtained for slopes between -4 and -3 as, $d_s = 6 + \text{slope}$. For instance, the decay in Figure 3 at low-q would reflect an extremely rough surface with a surface fractal dimension of 2.96.

In pyrolytic silicas, which are non-porous, a steep decay is seen at intermediate-q ($q>0.02$) with a power-law decay of -4 indicating the surface of primary particles following Porod's Law for surface scattering [6, 25], light circles in Figure 2. For $q<0.02Å^{-1}$, a mass-fractal aggregate regime is observed with a weaker power-law slope, here about -1.8 which corresponds with diffusion-limited-cluster-cluster aggregation (DLCA) [7, 18-20]. For pyrolytic silica, the dilute conditions and rapid reaction lead to *transport control* of growth and $d_f = 1.8$ [6].

Precipitated silica displays a similar Porod Regime at high-q ($q>0.02$) but a different mass-fractal regime of about -2.1 slope ($d_f = 2.1$) associated with *reaction-limited-clu*ster-cluster aggregation (RLCA) [7, 18-20]. In precipitated silica, cluster aggregation is again a major route to aggregate growth but the chemistry is slower leading to reaction-limited (denser) growth.

The bottom curve in Figure 2 shows an acid catalyzed silica aerogel powder produced using TEOS and supercritical extraction of $CO_2$ after solvent exchange [7, 27]. Primary particles are not observed in the available q-range (no power-law -4 regime), and the meso- to microporous structure is mass-fractal with a dimension of about -2.5 associated with diffusion-limited-monomer-cluster growth (DLMC) [7, 18-20].

In the control series of *ASG* powders, the *Reactor Configuration A samples* display scattering curves very similar to that of the supercritically extracted aerogel powders. In other

cases, such as in *Reactor Configuration C and Configuration B at high-TEOS/Water Ratio*, a change in growth mechanism from transport limited, mass-fractal growth to reaction limited, surface fractal growth is observed as reflected by a transition in slope in the mesoporous range (q=0.08) as discussed below and shown in Figure 2, upper of two ASG curves.

Both the ASG powders and the supercritically extracted aerogels display high specific surface areas by nitrogen adsorption using BET analysis: 500 to 700 $m^2/g$. The pyrolytic and precipitated silicas have surface areas in the 100 $m^2/g$ range that can be directly associated with the Porod regime and primary particle knee (following Guinier's Law) observed in Figure 2, $q > 0.02Å^{-1}$. At highest-q, $q > 0.2Å^{-1}$, for precipitated silica, produced in a solution process by acidification of sodium silicate, a deviation from the Porod regime can be seen in Figure 2 which may be related to a microporous structure within the primary particles.

For "q" larger than about 0.1 (corresponding to sizes below 5 nm in diameter) the ASG powders display a power-law decay weaker than -3 which is associated with objects of low-dimension, such as ramified, mass-fractal aggregates, Figure 3. Throughout this control series a power-law of -2.4 is consistently seen for $q > 0.1Å^{-1}$. Such a power-law decay is expected from diffusion-limited-monomer-cluster growth (DLMC) [7, 18-20]. A DLMC mechanism is reasonable for growth of silica particles at an early stage in the ASG reactor where small, reactive, partially condensed silica particles, less than 5Å in diameter, initially are limited by the transport of reactants and catalyst in the lateral diffusion dominated early stages of the mixing zone. This regime reflects the initial stages of growth where the reactant streams just begin to mix and condense into an aerosol. At lower-q, reflecting larger-sizes and later times of reaction, a transition to a different scaling-regime is often observed, especially in the less well mixed reactor configurations B and C, c.f. -3.04 slope in Figure 3. This may reflect changes in the growth process downstream in the mixing zone.

In this study, ASG powders display surface areas of about 400 to 600 $m^2/g$ as calculated using the BET method from nitrogen adsorption measurements. For silica, with a density of 2.2 $g/cm^3$, this would correspond to spherical particles with a radius of gyration of about 4 nm or "q"

of 0.08 $Å^{-1}$. This is roughly the q-range where the transition in scaling, discussed above and seen in Figure 3, is observed. This analysis is overly simplified since the bulk density of 2.2 $g/cm^3$ is too high for the molecular scale aggregates indicated at high-q (-2.4 slope at q>0.1), however, it serves as a rough approximation to explain the relationship between the scattering plot of Figure 3 and the BET values. The proximity of the scaling transition and a rough calculation of the primary particle size from the BET results indicates that the high-q mass-fractal structure displayed in most of the data is not accessible by nitrogen adsorption. This is because the diameter of $N_2$ is about 1.6 nm. This extremely small-scale, microporous structure has not been previously observed in other continuous process silicas such as pyrolytic silicas or commercial precipitated silicas and is reminiscent of some morphologies observed in supercritically extracted aerogels [24], as discussed above in Figure 2.

The low-q slope (-3.04 slope for q<0.1) is associated with mesopores which are observed by $N_2$ absorption. Figure 4 shows the pore size distribution measured from nitrogen adsorption experiments using BJH theory [26]. The sharp distribution centers around a pore radius of about 4 nm with the distribution in the mesoporous range, i.e. >2 nm. Such sharp, mesoporous distributions are characteristic of ASG nano-powders. The tabulated specific surface areas from the BET analysis, reported here, involve annealing (degassing) the powders at 250°C until a vacuum of less than 5 mmHg is achieved (4 to 6 hours).

Most of the ASG powders display the two power-law regimes seen in Figure 3. The q-value for the intersection of these two regimes can be calculated by extrapolation of the two power-laws which are fit locally using a least-squares method. The data is weighted using the propagated standard deviation from the raw data. If this q-value is interpreted as the transition point, an associated spherical radius of gyration can be calculated, $R_g = \pi/(1.3\ q_{intercept})$, where $q_{intercept}$ is the q-value at the intercept of the two power-laws. This can then be used in the unified equation [27, 28] to calculate the global scattering curve, the line in Figure 3. This calculated curve is based on a model using mass-fractal, microporous primary particles, formed early in the reactor, which make-up larger scale, mesoporous structures that are either surface-fractal, 3-d with extremely rough

surfaces, or mass-fractal with a dimension different than the microporous structure reflecting a transition in growth mechanism.

Figure 5 shows a schematic of the difference between a mass- and surface fractal for simplified aggregates. Although the morphological difference between extremely rough surfaces and dense mass-fractal morphologies may seem sublime, comparative data from this series of controlled powders indicates that there is a real effect in terms of BET surface areas associated with this transition in nano-structure.

*Reactor Configuration B*, TEOS and Water Bubbler Temperature Variation:

*Reactor Configuration B* will first be discussed since it displays a transition between the oxide growth mechanisms of *configurations C* and *A* as a function of the water/TEOS molar feed ratio. The laminar stream "a" in *Reactor Configuration B*, Figure 1, is water vapor which first forms an aerosol on cooling followed by nucleation of TEOS on these water droplets. Acidification of this mixture from stream "c" occurs further downstream than in *Reactor Configuration A* where acidified water first condenses, Figure 1. Table 3 shows that at high water/TEOS molar fractions, > 15, the mesopore structure is mass-fractal (power-law slope > -3) since the excess water facilitates acidification, and particle growth is transport rather than reaction limited. As the water/TEOS ratio is dropped in the direction of stoichiometric levels, 2, a mass- to surface-fractal transition is observed in the low-q power-law slope. This reflects decreased availability of HCl and a transition to denser, reaction-limited growth. HCl is transported to the reacting aerosol droplets by acidification of water. When insufficient HCl is present for complete hydrolysis of TEOS, the condensation reaction is slower because fewer condensable sites are available.

The transition from mass- to surface-fractal mesoporous structure in *Reactor Configuration B* powders is evidenced in the BET analysis by a drop in the specific surface area of more than 100 $m^2/g$ between the 75 and 80°C TEOS *Reactor Configuration B* powders. A calculation of the radius of gyration for spherical silica particles having the measured BET surface area (Table 3, parenthesis after BET value in Å) is close to the radius of gyration for the intercept of the two

power-law decays (also in Å), listed as the Transition $R_g$ in Table 3. The mass- to surface-fractal transition occurs at an estimated overall water/TEOS molar ratio between 17 and 13 in Table 3 (corresponding to a mass ratio of 1.5 to 1.1).

It is also possible to vary the water/TEOS ratio through variation of the water bubbler temperature. Increasing the partial pressure of water in *Reactor Configuration B* enhances condensation of the initial water aerosol since the outer stream is the water stream for *Reactor Configuration B*. A transition from surface to mass fractal scaling is observed at high-water content, near the 13 to 17 water/TEOS ratio observed in the TEOS heating runs for *Reactor Configuration B*, Table 4. There is also an associated increase in the specific surface area measured by BET in this range of water/TEOS ratio of about 100 $m^2$/gm. A similar explanation, based on enhanced availability of acid catalyst at high water fraction, can describe this behavior.

The 90°C water run in Table 4 does not fit with this explanation and may be due to excess water inhibiting the condensation reaction as discussed in the introduction. As noted above, this is a special problem with *Reactor Configuration B* at high-water concentrations since the outer stream, first to condense, is the water stream in this case.

Comparison of *Reactor Configurations A, B* and *C*

The arrangement of laminar flow streams, Figure 1, has an effect on powder nano-structure especially at low alkoxide concentrations (temperatures) as seen in Figure 6. At low TEOS concentrations *Reactor Configurations B* and *C* have distinguishable mesoporous structure (SAXS curves, open and light markers, diverge at low-q in Figure 6) while at high TEOS concentration, powders made in *Reactor Configurations B* and *C* are indistinguishable. The BET specific surface areas for both the *B* and *C* powders produced from a TEOS vapor stream at 90°C is about 515 $m^2$/g. The nano-structure of these two powders is identical as evidenced by overlapping SAXS curves in Figure 6. The two powders, *B* and *C*, diverge in structure at lower alkoxide concentrations (70°C TEOS) although the specific surface areas remain close (490 $m^2$/g). The sequence of low-q power-law, *A*, *B*, *C* in increasing power-law decay is seen over a range of intermediate TEOS temperatures as well, Figure 6, indicating that configuration *C* favors the

growth of denser, mesoporous structures, especially at high water/TEOS ratios. This can be explained by insufficient contact of water and HCl, limiting the hydrolysis reaction (see Figure 1 configurations).

In *Reactor Configuration B* water condenses first leading to a path for HCl migration through the TEOS stream. *Reactor Configuration A* offers a direct path for HCl to acidify the condensing water, leading to the most complete reaction and the lowest-density, mesoporous structures. The mesoporous structure from all powders produced in *Reactor Configuration A* are mass-fractal, Table 6. Tables 5 and 6 show mesoporous surface-fractal behavior for all of the *Reactor Configuration C* powders (>3) and mass-fractal behavior for all of the *Reactor Configuration A* powders (<3).

Figure 7 shows four SEM micrographs on a 10-micron scale for *Reactor Configuration A* and *B* powders. Generally, finer-scale agglomerates (upper micrographs) which form large particles on a 10-micron-scale (lower micrographs) result from mass-fractal mesoporous structure in these systems. That is, the highest-surface area, mass-fractal, mesoporous samples display the largest 10-micron scale particle size since these uniform, nano-scale structures packe well on a 10-micron scale. It is possible to mechanically or sonically break up these large agglomerates into sub-micron scale particles.

The water concentration (bubbler temperature) was varied only for *Reactor Configurations B* and *C* in this control series, Figure 8 and Tables 4 and 7. At 75°C (low water concentration) *Reactor Configuration C* displays a denser mesoporous structure (steeper low-q slope in Figure 8 and Table 4) consistent with the general trend for the TEOS temperature series comparison. At 80 and 85°C the *B* and *C* powders are similar in scattering profile and in BET surface area (Figure 8 and Tables 4 and 7). Of particular interest is the 90°C powder, noted above, which shows mesoporous surface-fractal scaling for *Reactor Configuration B* and mass-fractal scaling for *Reactor Configuration C* in this water temperature series. This is presumably due to excess water condensation in *Reactor Configuration B* where stream "a" is water (see Figure 1). Excess water may slow condensation in this case, leading to reaction limited growth as discussed in the

Introduction.

Table 7 lists the scattering and nitrogen adsorption results for water concentration variation in *Reactor Configuration C*. For the surface-fractal mesoporous sample (75°C water), the estimated transition $R_g$, in parenthesis after the SSA value, agrees with the observed power-law intercept. For the mass-fractal powders, however, these values diverge indicating that nitrogen can not penetrate to the smaller-scale features even in the mesoporous regime for these powders. (*Reactor Configuration B* water concentration series is shown in Table 4.)

The transition from mesoporous surface- to mass-fractal aggregates occurs at a lower overall molar water concentration in *Reactor Configuration C* (10 to 15) compared to *B* (15 to 23) because water is confined to the reaction zone in *C* (stream "c", Figure 1). This supports the idea of environmental loss of water from stream "a" in *Reactor Configuration B.*

Figure 9 shows a schematic summary of the microporous to mesoporous growth models for ASG powders under different reactor configurations based on the scattering and surface area measurements. Early stages of growth in all reactors can be describe by diffusion-limited-monomer-cluster growth which leads to a mass-fractal dimension of about 2.5 (2.4 is observed in the scattering data). In *Reactor Configurations B* and *C* there is a transition on the mesoporous scale to reaction-limited-monomer-cluster growth, leading to surface fractal structures (3-d structures). In *Reactor Configuration B* this transition can be mitigated by increasing the water/TEOS ratio which may serve to enhance catalyst transport to the reacting mixture and making the growth transport limited. This can be achieved in *Reactor Configuration C* only by increasing the water concentration (not by decreasing the TEOS concentration).

Infra-red Spectroscopy from ASG Powders:

Figure 10 shows IR spectra taken on ASG powders produced in *Reactor Configuration A* (TEOS 80°C, water 75°C) and *Configuration C* under the same conditions. In addition to standard bands associated with silica [7, p. 584-585] , labeled "Si-O" in Figure 10, a prominent band at just below 1000 $cm^{-1}$ is associated with SiOH and the moderately strong band at about 1600 $cm^{-1}$ is associated with water. In the top patterns, labeled 1-3, a moderate peak just below 1500 $cm^{-1}$

reflects C-H stretch from organic contaminants. This band can be associated with either ethanol byproduct or with non-hydrolyzed TEOS in the ASG powders. The C-H stretch can be removed by heating the powders to above 300°C (upper three spectra, 1-3) or by application of a vacuum (lower two spectra, 4-5). The top patterns, 1-3, were produced on powders which had been stored for several months, while the bottom patterns, 4 and 5, are from powders a few weeks old. This vacuum/aging effect seems to support organic species as the source of the C-H band.

As previously reported [1], the degassed and aged powders do not show significant carbon (<1%) by elemental analysis. The IR data indicates that the final ASG powders do not contain significant amounts of partially hydrolyzed TEOS. The final powders contain Si-OH groups in significant proportions which could be reactive in these systems. IR supports the proposition that, after condensation, mesoporous aggregates from partially hydrolyzed TEOS may further hydrolyze in the aggregates to form silanol groups due to the presence of water and trace amounts of HCl.

**Conclusions:**

Process control in the aero-sol-gel (ASG) reactor for production of nano-structured powders was investigated by variation of laminar-flow stream arrangement and reactant concentration in a controlled series of powders. The powders consistently display high specific surface areas of 400 to 700 $m^2/g$ by nitrogen adsorption and BET analysis and a narrow pore size distribution in the 4 nm range. The powders display both micro- as well as mesoporous structure by analysis of small-angle x-ray scattering data. A transition in growth mechanism is observed at about 4 nm which is modeled in terms of a transition from diffusion-limited-monomer-cluster growth to reaction-limited-monomer-cluster growth. Through manipulation of the reactor geometry and reactant concentrations it is possible to control the amount of reactive species in ASG powders.

Although a single precursor that produces highly reproducible powders is discussed in this paper, a number of alternative ASG reactants have been investigated. Further publications detailing these systems are planned in the near future.

**Acknowledgments:**

This work was supported by the National Science Foundation under a Research Initiation Award CTS 97-30535.

**References:**

1. Hyeon-Lee, J.; Beaucage; G., Pratsinis, S. E., *Chem. Mater.* **9**, 2400 (1997).
2. Hyeon-Lee, J.; Beaucage; G., Pratsinis, S. E., in MRS Symposium Series **520** "Nano-structured powders and their industrial applications", eds. Beaucage, G.; Mark, J. E., Burns, G. T.; Hua, D. W. Materials Research Society, Warrendale, PA, 115 (1998).
3. Pratsinis, S. E.; Zhu, W. ; Vemury, S. *Powder Technol.* **86**, 87 (1996).
4. Zhu, W., Pratsinis, S. E. In *Nanotechnology*, Chow, G. M., Gonsalves, K.E., Eds.; ACS Symposium Series **622**; American Chemical Society; Washington, DC, pp. 64-78 (1996).
5. Vemury, S.; Pratsinis, S. E. *Appl. Phys. Lett.,* **66**, 3275 (1995).
6. Hyeon-Lee, J.; Beaucage; G., Pratsinis, S. E.; Vemury, S., *Langmuir* **14**, 5751 (1998).
7. Brinker, C. J.; Scherer, G. W., "Sol-Gel Science", Academic Press, NY (1990).
8. Matijevic, E., and Visca, M. Ger. Offen. 2, 924,072, 20 December (1979).
9. Visca, M. and Matijevic, E., *J. Coll. Inter. Sci.*, **68**, 308 (1979).
10. Matijevic, E. in "*Heterogeneous Atmospheric Chemistry*", I. Schryer and R. David eds., American Geophysical Union, Washington, D. C. (1982).
11. Ingebrethsen, B. J.; Matijevic, E. and Partch, R. E. *J. Colloid and Interf. Sci.* **95**, 228 (1983).
12. Cortesi, P.; Donati, G. and Saggese, G. European Patent Application EP0117755 A2 (1984).
13. Rubio, J.; Oteo, J. L.; Villegas, M. and Duran, P. *J. Mater. Sci.* **32**, 643 (1997).
14. Kostic, E. M.; Kiss, S. J.; Boskovic, S. B. and Zec, S. P. *Am. Ceram. Soc. Bull.* **76**, 60 (1997).
15. Gablenz, S.; Voltzke, D.; Abicht, H. -P.; Newmann-Zdralek, J. *J. Mat. Sci. Let.* **17**, 537 (1998).
16. Ocana M., Fornes, V., Serna C. J., *Ceramics Inter.* **18**, 99 (1992).
17. E. Matijevic, Q. P. Zhong, R. E. Partch, *Aerosol Sci. and Tech.* **22**, 162 (1995).
18. Meakin, P. in "On Growth and Form", Eds. H. E. Stanley and N. Ostrowsky (Martinus-Nijhoff, Boston, p. 111 (1986).

19. Schaefer, D. W. MRS Bulletin, **8**, 22 (1988).

20. Witten, T. A.; Sanders, L. M., *Phys. Rev. Lett.* **47**, 1400 (1981).

21. Perry, R. H., Chilton, C. H., "Chemical Engineers Handbook, 5'th Ed.", McGraw-Hill Book Co. NY, p. 3-62 (1973).

22. Daniels, F.; Alberty, R. A., "Physical Chemistry, 4th ed.", John Wiley & Sons, NY, p.99 (1975).

23. Greg, S. J.; Sing, K. S. W., "Adsorption, Surface Area, and Porosity, 2nd ed.", Academic Press, NY, p. 25 (1982).

24. Beaucage, G., *J. Appl. Cryst.*, **28**, 717 (1995) and Beaucage, G.; Schaefer, D. W., *J. Non-Cryst. Solids*, **172-174** 797 (1994).

25. Schaefer, D. W.; Martin, J. E.; Keefer, K. D. in "Physics of Finely Divided Matter", Eds. N. Bocarra and M. Daoud, Springer-Verlag, Berlin (1985).

26. Barett, E. P.; Joyner, L. G.; Halenda, P. P., *J. Am. Chem. Soc.* **73**, 3737 (1951).

27. Beaucage, G., *J. Appl. Cryst.*, **29**, 134 (1996).

28. Beaucage, G.; Rane, S.; Sukumaran, S.; Satkowski, M. M.; Schectman, L. A.; Doi, Y., *Macromolecules*, **30**, 4158, (1997).

29. Hurd, A. J.; Schaefer, D. W.; Smith, D. M.; Ross, S. B.; Le Mehaute, A.; Spooner, S., *Phys. Rev. B*, **39**, 9742 (1989).

30. Bale, H. D.; Schmidt, P. W., *Phys. Rev. Lett.* **53**, 596 (1984).

31. Wong, P.; Bray, A. J., *J. Appl. Cryst.* **21**, 786 (1988).

32. The overall molar ratio for the mixing zone is estimated using the ideal gas law to approximate molar concentration of the reactants fed to the laminar flow chamber,

$$c_{Reactant} = n/V = P_{Vapor}/RT_{bubbler}, \qquad (1)$$

where R is 6.2361 x $10^{-2}$ $cm^3$ mmHg/(gmole °K) [33]. This concentration is given by,

$$c_{Reactant} = n_{Reactant}/(V_{N2} + V_{Reactant}) \qquad (2)$$

As the reactants are vaporized the volume of the feed streams increases by $V_{Reactant}$ in equation (2). Since the feed rate of nitrogen carrier gas is controlled, 45 $cm^3$/sec for all feed streams, it is desirable to obtain the number of moles of reactant per nitrogen volume, $c_{Reactant/N2} = n_{Reactant}/V_{N2}$, for calculation of the overall water/TEOS molar ratios. The reactor operates at atmospheric pressure, so the reactant volume from the bubbler is a linear

function of the number of moles of reactant, again, using the ideal gas approximation,

$V_{Reactant} = n_{Reactant}\ R\ T_{bubbler}/760\ mm\ Hg.$ (3)

Combining equations (1) to (3) we can estimate $c_{Reactant/N2}$, the molar concentration per volume $N_2$, as,

$c_{Reactant/N2} = 1/(RT_{bubbler}\ (1/P_{vapor} - 1/760\ mm\ Hg))$. (4)

Equation (4) is obtained from, the inverse of equation (2), using $V_{Reactant}/n_{Reactant}$ from equation (3) and the definition of $c_{Reactant}$ from equation (1),
$1/c_{Reactant} = V_{N2}/n_{Reactant} + V_{Reactant}/n_{Reactant} = 1/c_{Reactant/N2} + RT_{bubbler}/760\ mmHg = RT_{bubbler}/P_{vapor}$ rearrangement of the latter two expressions leads directly to equation (4).

Not all of this reactant is available to the reaction since the reaction/mixing zone will contain close to saturated vapors of the reactants at 25°C and atmospheric pressure. The loss in the reactor due to these 25°C non-condensable vapors per $N_2$ volume, $c_{loss}$, is given by,

$c_{loss} = 1/(R\ 298°K\ (1/P_{vapor\ 298} - 1/760\ mm\ Hg))$. (5)

The overall number of moles available to the reaction per cubic centimeter of nitrogen is $c_{Reactant/N2} - c_{loss}$. The ratio of overall concentration per cubic centimeter nitrogen between water and TEOS is reported in Tables 1 and 2 as a function of TEOS temperature and water temperature. This approach assumes the ideal gas law applies to these vapor streams and is meant to give a rough idea of the overall molar feed ratios involved in the ASG reactor. Losses by dilution to room air are ignored in the calculation of approximate concentration ratios.

33. Perry, R. H. and Chilton, C. H., " Chemical Engineers Handbook 4'th edition", McGraw Hill Book Company, NY (1973).

**Table Captions:**

**Table 1.** Vapor Pressure of water and overall molar ratio of reactants in the mixing zone for a TEOS stream at 85°C [21 (p. 3-45), 32].

**Table 2.** Vapor Pressure of TEOS and overall molar ration of reactants in the mixing zone for a water stream at 75°C [22, 32].

**Table 3.** Scattering and gas adsorption results for *Reactor Configuration B* varying TEOS concentration (water 75°C).

**Table 4.** Scattering and gas adsorption results for *Reactor Configuration B* varying water concentration (TEOS 85°C).

**Table 5.** Scattering results for *Reactor Configuration C* varying TEOS concentration (water 75°C).

**Table 6.** Scattering results for *Reactor Configuration A* varying TEOS concentration (water 75°C).

**Table 7.** Scattering and gas adsorption results for *Reactor Configuration C* varying water concentration (TEOS 85°C).

**Tables:**

Table 1. Vapor Pressure of water and overall molar ratio of reactants in the mixing zone for a TEOS stream at 85°C [21 (p. 3-45), 32].

| Temperature | Water Vapor Pressure | $(c - c_{loss})_{water/N2}$ | $H_2O$/TEOS |
|---|---|---|---|
| ℃ | mm Hg | gmole/$cm^3$ $N_2$ | 85°C TEOS |
| *25* | *23.756* | *0* | |
| 70 | 233.7 | 14.46 | 7.7 |
| **75** | **289.1** | 20.18 | **10.8** |
| 80 | 355.1 | 28.96 | 15.4 |
| 85 | 433.6 | 43.90 | 23.4 |
| 90 | 525.8 | 74.06 | 39.5 |
| 95 | 633.9 | 165.16 | 88.0 |

Table 2. Vapor Pressure of TEOS and overall molar ration of reactants in the mixing zone for a water stream at 75°C [22, 32].

| Temperature | TEOS Vapor Pressure | $(c - c_{loss})_{TEOS/N2}$ | $H_2O$/TEOS |
|---|---|---|---|
| °C | mm Hg | gmole/cm$^3$ $N_2$ | 75°C Water |
| *25* | *1.9* | *0* | |
| 70 | 21.3 | 0.922 | 21.9 |
| 75 | 26.8 | 1.18 | 17.1 |
| 80 | 33.5 | 1.49 | 13.5 |
| **85** | **41.7** | **1.88** | **10.8** |
| 90 | 51.6 | 2.35 | 8.6 |

Table 3. Scattering and gas adsorption results for *Reactor Configuration B* varying TEOS concentration (water 75°C).

| TEOS °C | Low-q Power Law | $N_2$ SSA $m^2/g$ (Sphere $R_g$, Å) | Transition $R_g$ (Å) | $H_2O$/TEOS (molar ratio) |
|---|---|---|---|---|
| 70 | 2.84 ± 0.003 | 492 (21) | 23.2 | 21.9 |
| 75 | 2.97 ± 0.01 | 602 (17) | 26.1 | 17.1 |
| 80 | 3.08 ± 0.01 | 467 (23) | 21.5 | 13.5 |
| 85 | 3.16 ± 0.001 | 398 (26) | 20.3 | 10.8 |
| 90 | 3.04 ± 0.02 | (No Data) | 23.4 | 8.6 |

Table 4. Scattering and gas adsorption results for *Reactor Configuration B* varying water concentration (TEOS 85°C).

| $H_2O$ °C | Low-q Power Law | $N_2$ SSA $m^2/g$ (Sphere $R_g$, Å) | Transition $R_g$ (Å) | $H_2O$/TEOS (molar ratio) |
|---|---|---|---|---|
| 75 | 3.16 ± 0.001 | 398 (26) | 20.3 | 10.8 |
| 80 | 3.13 ± 0.002 | 468 (22) | 18.6 | 15.4 |
| 85 | 2.98 ± 0.002 | 546 (19) | 20.2 | 23.4 |
| *90* | *3.16 ± 0.001* | *592 (18)* | *20.9* | *39.5* |

Table 5. Scattering results for *Reactor Configuration C* varying TEOS concentration (water 75°C).

| TEOS °C | Low-q Power Law | $N_2$ SSA $m^2/g$ (Sphere $R_g$, Å) | Transition $R_g$ (Å) | $H_2O$/TEOS (molar ratio) |
|---|---|---|---|---|
| 70 | 3.21 ± 0.004 | 489 | 17.5 | 21.9 |
| 75 | 3.29 ± 0.001 | 453 | 24.9 | 17.1 |
| 80 | 3.40 ± 0.001 | 491 | 26.6 | 13.5 |
| 85 | 3.04 ± 0.002 | 507 | 21.7 | 10.8 |
| 90 | 3.05 ± 0.02 | 514 | 24.5 | 8.6 |

Table 6. Scattering results for *Reactor Configuration A* varying TEOS concentration (water 75°C).

| TEOS ℃ | Low-q Power Law | $N_2$ SSA $m^2/g$ | Transition $R_g$ | High-q Power | $H_2O$/TEOS |
|---|---|---|---|---|---|
| 70 | 2.45 ± 0.003 | 419 | 11.9 | 2.4 (Fixed) | 21.9 |
| 80 | 2.21 ± 0.003 | 559 | ----- | 2.4 (Fixed) | 13.5 |
| 90 | 2.43 ± 0.003 | 519 | ----- | 2.50 ± 0.01 | 8.6 |

Table 7. Scattering and gas adsorption results for *Reactor Configuration C* varying water concentration (TEOS 85°C).

| $H_2O$ °C | Low-q Power Law | $N_2$ SSA $m^2/g$ (Sphere $R_g$, Å) | Transition $R_g$ (Å) | $H_2O$/TEOS (molar ratio) |
|---|---|---|---|---|
| 75 | 3.29 ± 0.001 | 453 (23) | 24.9 | 10.8 |
| 80 | 2.81 ± 0.002 | 530 (20) | 6.61 | 15.4 |
| 85 | 2.95 ± 0.001 | 493 (21) | 15.4 | 23.4 |
| *90* | *2.82 ± 0.003* | *561 (19)* | *15.8* | *39.5* |

**Figure Captions:**

**Figure 1.** Schematic of thermally controlled, laminar flow assembly for ASG reactor. Reactant streams enter at the bottom of the concentric tubes from temperature controlled bubblers using dry nitrogen as a carrier gas. Laminar flow streams exit at the top into the mixing zone where the reaction takes place.

**Figure 2.** Comparison of scattering from the control series ASG silica powders (two black curves), pyrolytic (from reference [6]), precipitated (Hi-Sil), and a supercritically extracted aerogel powder (from Carol Ashley at Sandia National Laboratories [27]). Both pyrolytic and precipitated silicas display a Porod decay, -4 slope at high-q.

**Figure 3.** Typical data set for ASG powders. TEOS 90°C, water 75°C *Reactor Configuration B.* Line is unified calculation as discussed in the text [27, 28].

**Figure 4.** Pore Volume Distribution from BET analysis of nitrogen adsorption data. Data shown are from *Reactor Configuration A* TEOS 85°C, water 75°C.

**Figure 5.** Schematic of mass- and surface-fractal aggregates. For ASG powders, primary spheres (circles above) are themselves microporous, mass-fractal aggregates with $d_f = 2.4$ (not shown). In this work, surface-fractal, mesoporous structures display about $100 m^2/g$ less specific surface area than comparable mass-fractal structures.

**Figure 6.** Variability in structure with TEOS temperature and laminar flow arrangement. *Reactor Configurations A, B* and *C* for water bubbler temperature 75°C.

**Figure 7.** SEM micrographs of *Reactor Configuration A* (left 2) and *B* (right 2). *Reactor Configuration A*: TEOS 80°C Water 75°C, 559 $m^2/g$ mesopore mass-fractal $d_f \approx 2.4$. *Reactor Configuration B*: TEOS 85°C Water 75°C, 398 $m^2/g$, mesopore surface-fractal (-3.16 power-law from Table 3 ) $d_s = 2.84$. Micrographs are courtesy of Doug Kohls.

**Figure 8.** Variable structure with water temperature and laminar flow arrangement.

**Figure 9.** Schematic of growth mechanism models for this control series of TEOS based powders from the ASG reactor.

**Figure 10.** IR Spectra from ASG Powders. Lower two curves (4 and 5) from 5% silica in KBr

pellets subjected to vacuum for 10 minutes. Top three curves (1-3) are pure pressed ASG silica not subjected to vacuum. Both series were subjected to purging in a dry inert gas for 30 minutes prior to IR scan. (Bands are assigned following reference [7] p. 584-585.)

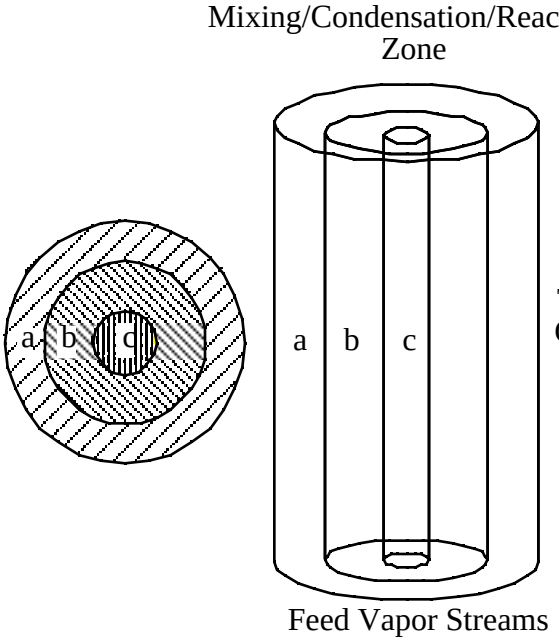


| Laminar Stream | Reactor Configuration A | B | C |
|---|---|---|---|
| a | HCl | Water | HCl |
| b | Water | TEOS | TEOS |
| c | TEOS | HCl | Water |

Figure 1. Schematic of thermally controlled, laminar flow assembly for ASG reactor. Reactant streams enter at the bottom of the concentric tubes from temperature controlled bubblers using dry nitrogen as a carrier gas. Laminar flow streams exit at the top into the mixing zone where the reaction takes place.

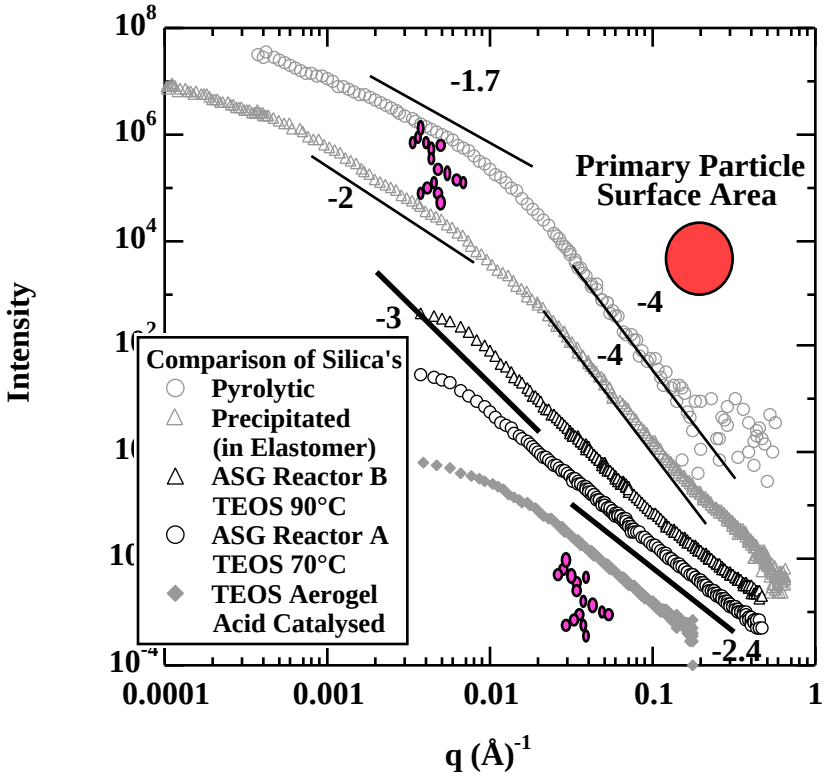


Figure 2. Comparison of scattering from the control series ASG silica powders (two black curves), pyrolytic (from reference [6]), precipitated (Hi-Sil), and a supercritically extracted aerogel powder (from Carol Ashley at Sandia National Laboratories [27]). Both pyrolytic and precipitated silicas display a Porod decay, -4 slope at high-q.

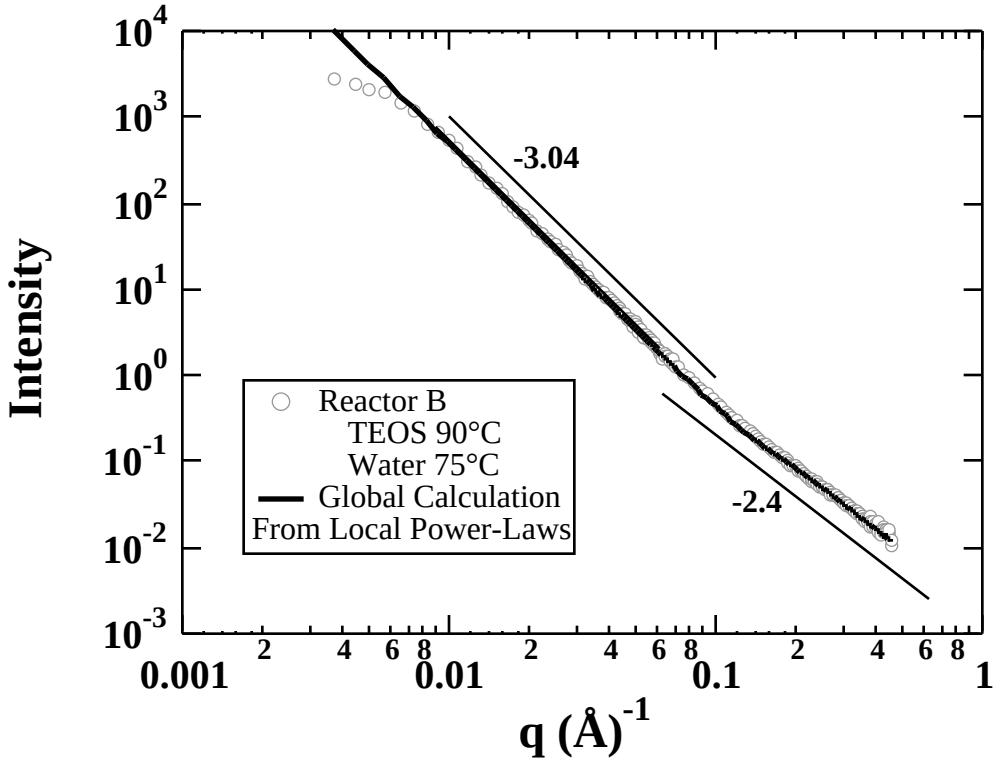


Figure 3. Typical data set for ASG powders. TEOS 90°C, water 75°C *Reactor Configuration B.* Line is unified calculation as discussed in the text [27, 28].

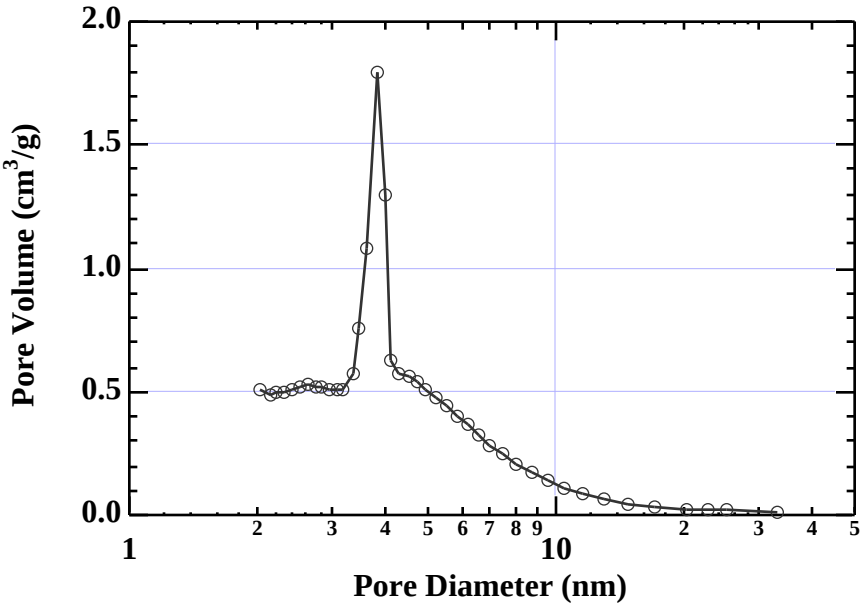


Figure 4. Pore Volume Distribution from BET analysis of nitrogen adsorption data. Data shown are from *Reactor Configuration A* TEOS 85°C, water 75°C.

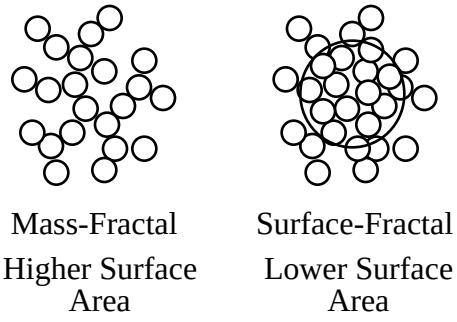


Figure 5. Schematic of mass- and surface-fractal aggregates. For ASG powders, primary spheres (circles above) are themselves microporous, mass-fractal aggregates with $d_f = 2.4$ (not shown). In this work, surface-fractal, mesoporous structures display about $100 m^2/g$ less specific surface area than comparable mass-fractal structures.

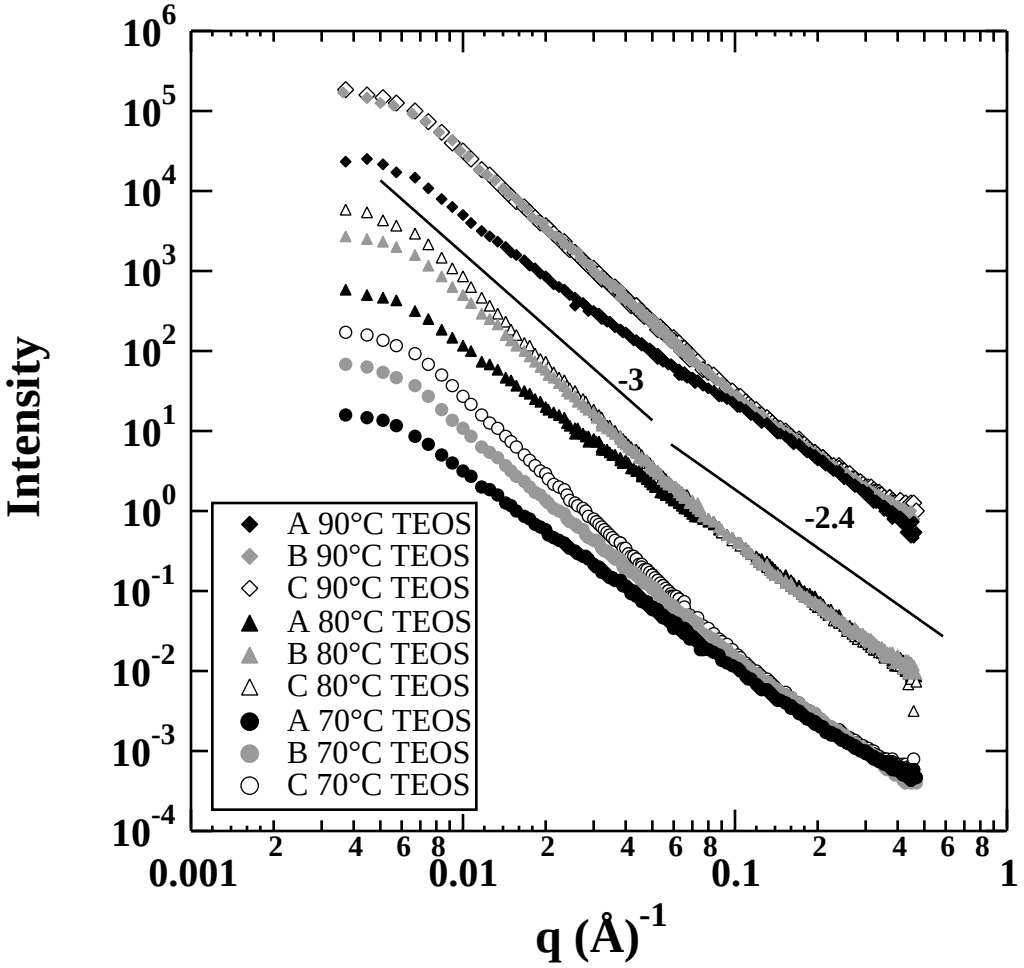


Figure 6. Variability in structure with TEOS temperature and laminar flow arrangement. *Reactor Configurations A, B* and *C* for water bubbler temperature 75°C.

***Insert Figure 7.***

Figure 7. SEM micrographs of *Reactor Configuration A* (left 2) and *B* (right 2). *Reactor Configuration A*: TEOS 80°C Water 75°C, 559 $m^2/g$ mesopore mass-fractal $d_f \approx 2.4$. *Reactor Configuration B*: TEOS 85°C Water 75°C, 398 $m^2/g$, mesopore surface-fractal (-3.16 power-law from Table 3 ) $d_s = 2.84$. Micrographs are courtesy of Doug Kohls.

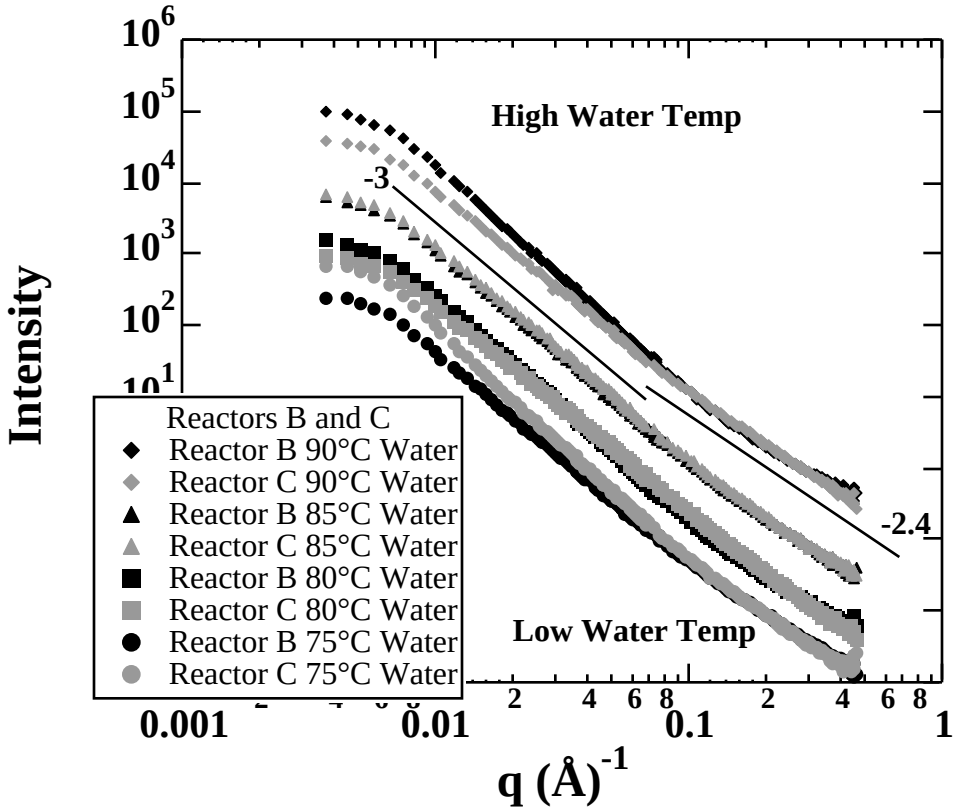


Figure 8. Variable structure with water temperature and laminar flow arrangement.

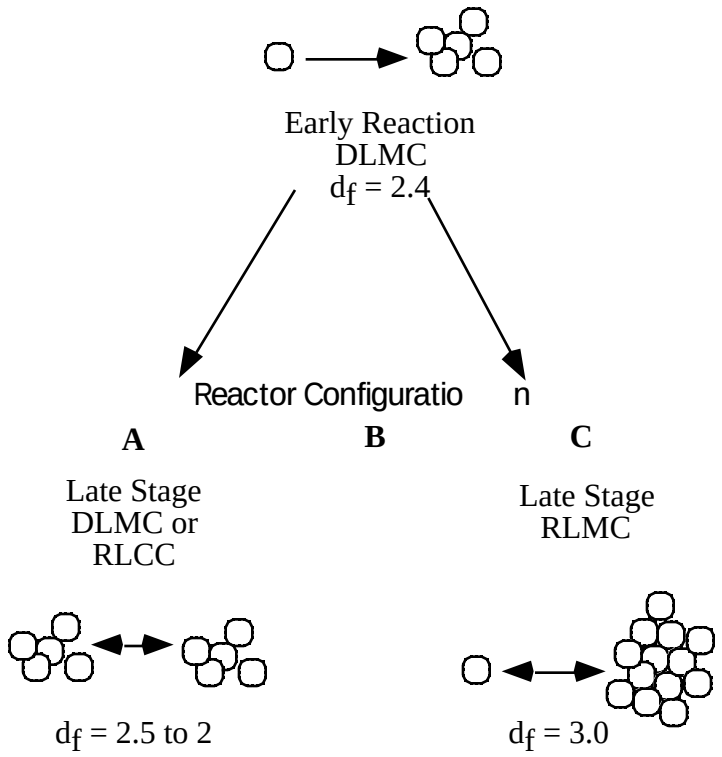


Figure 9. Overview cartoon of growth mechanism models for this control series of TEOS based powders from the ASG reactor.

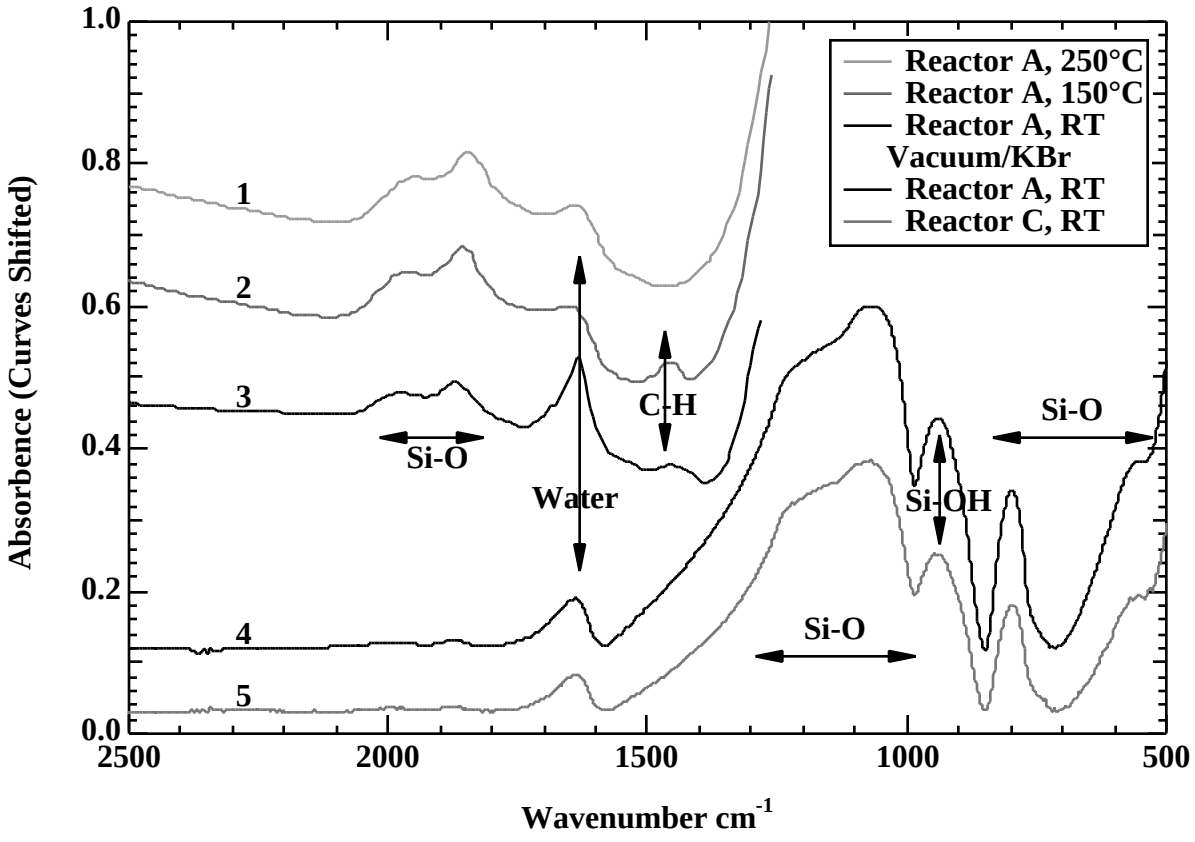


Figure 10. IR Spectra from ASG Powders. Lower two curves (4 and 5) from 5% silica in KBr pellets subjected to vacuum for 10 minutes. Top three curves (1-3) are pure pressed ASG silica not subjected to vacuum. Both series were subjected to purging in a dry inert gas for 30 minutes prior to IR scan. (Bands are assigned following reference [7] p. 584-585.)